

Exploring Visual Patterns in Projected Human and Machine Decision-Making Paths*

ANDREAS HINTERREITER, CHRISTIAN STEINPARZ, MORITZ SCHÖFL, HOLGER STITZ, and MARC STREIT, Johannes Kepler University Linz, Austria

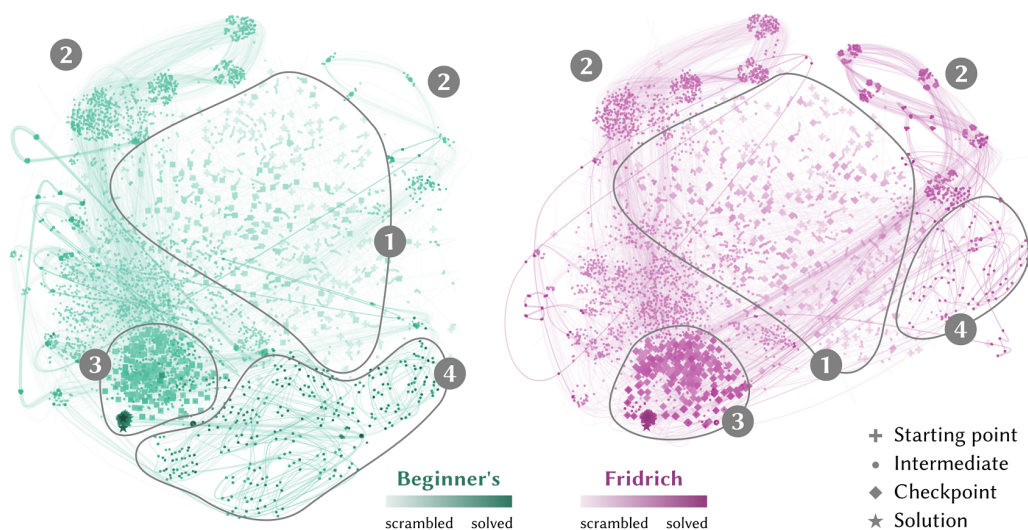


Fig. 1. Projected solution pathways for 100 random Rubik's Cubes solved with the beginner's method (left), and with Fridrich's method (right), respectively. Data for both algorithms was combined for the calculation of the t -SNE projection, but is shown in two individual visualizations for easier interpretation. The random initial states form a broad cluster near the center of the projected state space (1). Both solution algorithms take similar intermediate paths (2), and later checkpoints cluster densely near the final solution (3). Notably, Fridrich's algorithm avoids lengthy sequences of rotations to transform an almost solved cube into a solved cube (4).

In problem solving, the paths towards solutions can be viewed as a sequence of decisions. The decisions, made by humans or computers, describe a trajectory through a high-dimensional representation space of the problem. Using dimensionality reduction, these trajectories can be visualized in lower dimensional space. Such embedded trajectories have previously been applied to a wide variety of data, but so far, almost exclusively

*This paper is an extended version of the workshop paper "Visualization of Rubik's Cube Solution Algorithms" [51].

Authors' address: Andreas Hinterreiter, andreas.hinterreiter@jku.at; Christian Steinparz, christian.steinparz@jku.at; Moritz Schöfl, moritz.schoefl@jku.at; Holger Stitz, holger.stitz@jku.at; Marc Streit, marc.streit@jku.at, Johannes Kepler University Linz, Altenberger Straße 69, Linz, Austria, 4040.

Permission to make digital or hard copies of all or part of this work for personal or classroom use is granted without fee provided that copies are not made or distributed for profit or commercial advantage and that copies bear this notice and the full citation on the first page. Copyrights for components of this work owned by others than ACM must be honored. Abstracting with credit is permitted. To copy otherwise, or republish, to post on servers or to redistribute to lists, requires prior specific permission and/or a fee. Request permissions from permissions@acm.org.

© 2018 Association for Computing Machinery.

2160-6455/2018/1-ART1 \$15.00

<https://doi.org/10.1145/1122445.1122456>

the self-similarity of single trajectories has been analyzed. In contrast, we describe patterns emerging from drawing many trajectories—for different initial conditions, end states, or solution strategies—in the same embedding space. We argue that general statements about the problem solving tasks and solving strategies can be made by interpreting these patterns. We explore and characterize such patterns in trajectories resulting from human and machine-made decisions in a variety of application domains: logic puzzles (Rubik’s cube), strategy games (chess), and optimization problems (neural network training). In the context of Rubik’s cube, we present a physical interactive demonstrator that uses trajectory visualization to provide immediate feedback to users regarding the consequences of their decisions. We also discuss the importance of suitably chosen representation spaces and similarity metrics for the embedding.

CCS Concepts: • **Human-centered computing** → **Visualization techniques**; *Information visualization*; *Visualization systems and tools*; • **Computing methodologies** → *Visual analytics*.

Additional Key Words and Phrases: algorithm visualization, game visualization, dimensionality reduction, trajectories, multivariate time series

ACM Reference Format:

Andreas Hinterreiter, Christian Steinparz, Moritz Schöfl, Holger Stitz, and Marc Streit. 2018. Exploring Visual Patterns in Projected Human and Machine Decision-Making Paths. *ACM Trans. Interact. Intell. Syst.* 1, 1, Article 1 (January 2018), 29 pages. <https://doi.org/10.1145/1122445.1122456>

1 INTRODUCTION

The act of solving problems usually involves sequences of decisions. In most contexts, decisions can be viewed as transitions between states in a representation space. For example, solving logic puzzles such as the Rubik’s cube requires decisions about how to transform an object from a random initial configuration to a solved final state. Strategy games can also be viewed as a progression through game states; each decision transforms the board state and leads closer to a player’s victory or defeat. Even optimization processes, such as the training of neural networks, involve decisions about transitioning from one intermediate state to another, with the hope that the process ultimately converges to a final solution.

In many applications domains, the decisions determining a transition from one state to another are decisions made consciously by human agents, often after a complex reasoning process. In other cases, the transitions between states can be based on decisions made automatically by algorithms. Examining patterns in the paths towards a problem solution can lead to a better understanding of approaches used by humans and machines to solve complex tasks.

For almost all real-world problems, the possible representation spaces are not only vast, but also high-dimensional. Many attributes are needed to accurately describe each intermediate state along the pathway to a solution. The high dimensionality of the state spaces makes assessing patterns in solution paths challenging. Previously, dimensionality reduction techniques have been used in conjunction with trajectory visualizations to explore high-dimensional sequences of states [4].

Research so far has mostly focused on discovering patterns based on self-similarity of single solution paths. However, the exact path towards a solution may depend strongly on the initial state for that particular instance of the problem. For example, in case of optimization algorithms, paths of convergence might depend on the chosen initialization. In other domains, such as in strategy games like chess, the initialization is always the same. Here, early decisions might force the solution path along one particular of many different tracks.

In both cases, viewing single solution paths without the context of many other paths can hide interesting patterns. In this paper, we present an extension of established trajectory techniques for visualizing high-dimensional paths through complex representation spaces. We identify patterns emerging from *multiple* projected solution trajectories. Using interactive visualization, we allow users to find such patterns and explore their relationship with the underlying real-world processes.

We present a general interactive prototype for the visualization of multiple high-dimensional solution trajectories and show how minimal adaptations can make this prototype useful in a diverse range of application domains. Specifically, we present examples for comparing Rubik’s cube solution algorithms, finding patterns in chess games, and assessing meaningful representations of neural network training processes. These examples show how extending the self-similarity concept of single projected solution trajectories to similarities between multiple trajectories can provide more insight into problem solving processes.

2 RELATED WORK

In our work, we study patterns emerging from multiple dimensionality-reduced trajectories through a problem state space. We will first discuss the general importance of trajectories for time series visualization. We will then briefly review the most widely used dimensionality reduction techniques. Finally, and most pertinently to our approach, we will discuss previous attempts on using trajectories for visualizing dimensionality-reduced data.

2.1 Trajectories for Time Series Visualization

Visualizing the progression of processes (algorithms, games, etc.) through different states is equivalent to visualizing multivariate time series data. A dataset with two quantitative attributes that change over time can be readily visualized as a trajectory through 2D data space, with time varying between the support points. The DimpVis system [31], for instance, demonstrated the use of trajectories as an important factor in interactive displays of time series data.

Trajectories naturally play an important role in visual analytics of movement [2]. When many trajectories (also known as trails) are shown at once, visual clutter can be a problem. To alleviate this issue, edge bundling techniques [15, 27] have been adapted to trail visualization [12, 29, 45]. For gaining additional insights from spatial trajectories, numerous trajectory data mining techniques have been developed [62].

2.2 Dimensionality Reduction

If the data to be visualized as trajectories has more than two attributes, applying dimensionality reduction is inevitable. A multitude of dimensionality reduction techniques has been developed [59], and their usefulness for data visualization has been studied [13]. Principal component analysis (PCA) and multidimensional scaling (MDS) are two classic techniques used for dimensionality reduction. In the 2000s, Isomap [53] and *t*-distributed stochastic neighbor embedding (*t*-SNE) [58] were presented—two non-linear techniques specifically created for data visualization. Around the same time, deep autoencoder networks have proven to be capable of learning low-dimensional codes of high-dimensional data [25]. More recently, uniform manifold approximation and projection (UMAP) was introduced as an alternative to *t*-SNE [40]. In the last years, projection techniques have been used increasingly for visualizations in explainable AI [26]. Rauber et al., for instance, used *t*-SNE for visualizing how the activity of neural networks evolves throughout training [47].

2.3 Combining Dimensionality Reduction and Trajectories

As stated above, trajectories can only readily be used for visualizing time series with two attributes. For time series with more attributes, a combination of dimensionality reduction with trajectory visualization can be a powerful approach.

In TimeSeriesPath, data points of multivariate time series are projected using principal component analysis (PCA), and shown as trajectories in 2D space [5]. Schreck et al. used self organizing maps (SOMs) to display projected trajectories of high-dimensional, time-resolved financial data [49]. In

ThermalPlot [52], multi-attribute time-series data is reduced to a single point by means a user-defined degree-of-interest (DOI) function and plotted in a DOI space. Items with similar temporal development are clustered and show similar trajectories. The Time Curve idiom by Bach et al. is “based on the metaphor of folding a timeline visualization into itself so as to bring similar time points close to each other” [4]. Time Curves are trajectories constructed from high-dimensional states via multidimensional scaling (MDS).

One example application in the Time Curves paper is the visualization of document edit histories [4]. In this domain, similar approaches had been used previously, by treating sequences of n -grams similarly to multivariate time series. Using PCA and differentiation, Mao et al. derived visualizations of n -gram data akin to phase space trajectories used in theoretical physics [39]. Ward and Guo generalized the notion of n -grams to non-textual data, yielding a shape-space representation of snippets of time series data [60]. The shape-space representation was, in turn, projected by PCA and visualized as trajectories in two dimensions.

In an approach very similar to Time Curves, van den Elzen et al. used t -SNE, among other projection techniques, to visualize high-dimensional states of dynamic networks [57]. A recent Master’s thesis [7] features similar visualizations of network states.

Rauber et al. [47] used t -SNE to visualize the activations in neural networks over time. In ModelSpace, Brown et al. [8] visualize user interaction data as projected trajectories, aiming to reveal patterns in the users’ intentions. Cakmak et al. used a t -SNE visualization for trend and outlier detection in projected time series [9]. Zhu and Chen created dimensionality-reduced trajectories for basketball games, making use of landmark MDS [63].

Finally, He and Chen used a time-aware implementation of t -SNE to visualize temporal patterns in representation data [23]. This temporal t -SNE variant places similar high dimensional states at large distances in the embedding spaces, if the are temporally far away from each other.

2.4 Context of This Work

Among these related works, the Time Curves paper by Bach et al. [4] is perhaps the most relevant one for our work. The authors described several characteristics of projected trajectories, such as point density and irregularity, as well as patterns such as transitions, cycles, and oscillations [4]. However, they focused on the interpretation of single trajectories and only hinted at the power of constructing and interpreting multiple trajectories together. We build upon their classification, but focus on additional patterns emerging from *multiple* trajectories.

Other authors have partially demonstrated the potential of constructing multiple trajectories in the same embedding space. Zhu and Chen could detect outlier games from among multiple basketball games [63]. Brown et al. discovered differences in velocities along multiple trajectories from interaction data, and traced back these differences to varying user speeds [8]. However, not much work has been done on identifying general patterns emerging from multiple embedded trajectories throughout different application domains.

In this paper we apply our approach on data from diverse application domains, including games (chess), puzzles (Rubik’s cube), and AI (neural network training). Depending on the application context, the number of trajectories we plot conjointly in the same embedding space varies between only a few and several hundreds. We argue that from similarities between multiple trajectories, general statements about the visualized decision-making processes can be made.

3 TECHNIQUE

Prior to visualizing paths of problem solutions with trajectories through an embedding space, a number of important decisions have to be made. The visualization depends strongly on how the real-world states are represented as vectors. The distance metric for these vectors needs to be

chosen carefully, as must the dimensionality reduction technique. Finally, a suitable visual encoding for the low-dimensional states and trajectories needs to be chosen. We discuss all these aspects in the following section. We also present a discussion of possible patterns emerging from multiple trajectories in the same embedding space.

3.1 State Space Representation

As described in the previous sections, our visualization approach is similar to the Time Curve technique introduced by Bach et al. [4]. Time Curves are trajectories drawn through projections of high-dimensional data points. They are constructed by defining a distance metric on the high-dimensional domain, and embedding the data points in two dimensions in such a way that certain characteristics of the high-dimensional distance metric are preserved. The projected points are connected depending on the timestamps associated with each high-dimensional data point. Table 1 lists the key terms and definitions in the context of dimensionality-reduced trajectories.

For the placement of the projected points in the embedding space, the points' timestamps do not matter. Only the relative temporal ordering is used for connecting the embedded points. In most scenarios, projected trajectories are thus visualizations of sequences (or ordered sets) of states. As such, this trajectory technique can be applied to any process that involves an object undergoing several sequential states, and state indices can entirely replace actual timestamps. Bach et al. use the term “data snapshot” to refer to the individual, high-dimensional data items that—together with the timestamps—make up the multivariate time series. They call the pairs of timestamps and data snapshots *time points*. In contrast, we refer to data snapshots as *states*, and we call the snapshot domain *state space*. This should stress our focus on sequential processes, in which the actual time values are not necessarily of interest or are not even available (such as in the guiding example below).

An essential requirement for constructing a meaningful visualization of trajectories through an embedding space is the way in which the real-world object (that goes through the sequential steps) is “digitized”. In our opinion, this is the first, and possibly most important decision when combining projection with trajectories, but it was not discussed in detail by Bach et al. We refer to this digitization as *state space representation*, and define it as a mapping from the “real world” \mathcal{R} to the state space \mathcal{S} . Importantly, the state space representation directly influences the meaning of any potential distance metrics. There can be many different choices regarding which of the object's attributes to include in the state space representation. Everything that is not included is potentially interesting *metadata*. While this metadata is not directly included in the calculation of the trajectories' support points, it can be encoded additionally, e. g. by coloring trajectories or points categorically depending on the associated metadata. In this sense, the actual value of the timestamp t_i of a time point (t_i, s_i) can be treated as metadata as well.

As a guiding example throughout this section, we apply our visualization approach to data from two well-known sorting algorithms: bubble sort and quicksort. We first create all possible permutations of the list $(1, \dots, n)$ for a given length n . We apply each of the two algorithms to each permutation and record all intermediate steps. For visualizing the progression of the algorithms, we first need to convert the list objects from \mathcal{R} to a suitably chosen state space \mathcal{S} by means of the state space representation r . We decide that we want to compare lists in terms of “how shuffled” they are. This similarity can be measured using an edit distance. There are now two approaches for obtaining meaningful distances:

- We can directly use the symmetric group of all permutations of lists with length n as our state space, i. e. $\mathcal{S} = \mathfrak{S}_n$. This would allow us to simply use an edit distance of our choice as metric d , such as the Hamming distance or the Damerau-Levenshtein distance.

Table 1. Key terms and definitions for the construction of Time Curves as given by Bach et al. [4], with our own notations for state space representations and dimensionality reduction.

Notation	Explanation
$t_i \in \mathbb{R}$	timestamp
\mathbb{S}	snapshot domain (state space)
$s_i \in \mathbb{S}$	data snapshot (state)
$p_i = (t_i, s_i)$	time point
$P = \{p_1, \dots, p_n\}$	temporal dataset
$d: \mathbb{S}^2 \rightarrow \mathbb{R}^+$	distance metric
$D = [d_{ij}] = [d(p_i, p_j)]$	distance matrix
$P_D = \{P, D\}$	temporal similarity dataset
$r: \mathcal{R} \rightarrow \mathbb{S}$	state space representation
$f: \mathbb{S} \rightarrow \mathbb{R}^2$ or $f: \mathbb{S}^n \rightarrow (\mathbb{R}^2)^n$	embedding*

* Domain and codomain of the embedding function depend on the chosen technique.

- Alternatively, we can use another representation of our lists, in which a distance of our choice (such as the squared euclidean distance) corresponds to an edit distance. In case of our permuted lists, such a representation could be constructed by performing a one-hot encoding, i.e. $\text{enc}((x_1, \dots, x_n)) = \text{flat}(\text{sparse}_n(x_1), \dots, \text{sparse}_n(x_n))$. Here, $\text{flat}(M)$ flattens a matrix M to a vector. The vector $\text{sparse}_n(i) = (\delta_{1i}, \dots, \delta_{ni})$ is a vector of length n in which only the i th entry is set to 1, and all other entries are set to 0. In the formula for $\text{sparse}_n(i)$, δ represents the Kronecker delta. The resulting vectors have a length of n^2 , and the state space is $\mathbb{S} = \{0, 1\}^{(n^2)}$. In this state space, $d(a, b) = \text{Euclidean}(a, b)^2 / 2$ is exactly equivalent to the Hamming distance.

While the first approach seems more straightforward, the second approach is often favourable from an implementation point of view. Many implementations of dimensionality reduction techniques offer the option to use custom distance metrics, but they often only work on numerical data.

3.2 Dimensionality Reduction

In this work, we focus on visualizing *multiple* trajectories conjointly. This also affects the calculation of the embedding used for dimensionality reduction. In order to embed all trajectories in the same space, the individual states of all sequences need to be projected in conjunction. This means that equal elements in the high-dimensional state space are more likely to occur multiple times. This is especially the case when the visualized real-world process is constrained to always start from the same initial state, always ends in the same final state, or has fixed intermediate states that need to be traversed (see also the discussion of patterns in Section 3.3). In our guiding example, each application of either of the two sorting algorithms terminates in the same state, namely the sorted array $(1, \dots, n)$. This state will be present in our dataset a total of m times, where m is the number of different initial states, multiplied by the number of sorting algorithms that are used. Most nonlinear embedding techniques do not map equal input states to equal output states, but instead to a cluster of slightly different output states. We need to decide whether to remove duplicates prior to the embedding routine, i.e. use each state only once. In many cases, this leads to a significantly smaller embedding space. Alternatively, we can include the duplicates, and rely on the embedding routine to cluster them closely together. This can highlight and—depending on the projection technique—offset points that are more often visited than others.

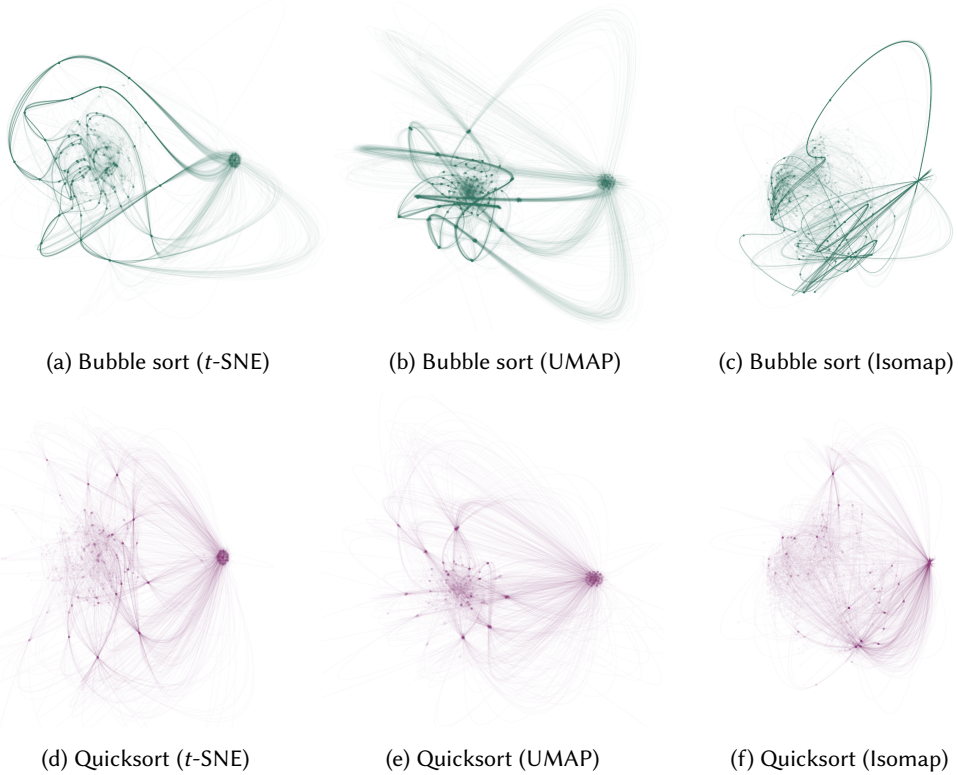


Fig. 2. Sorting trajectories for bubble sort (a–c) and quicksort (d–e), applied to all permutations of a list of length 6 with unique entries. Three different dimensionality reduction techniques are shown: (a, d) t -SNE with a perplexity of 100 and an exaggeration factor of 2 during the main optimization; (b, e) UMAP with 25 nearest neighbors and a minimum distance of 0.1; and (c, f) Isomap with 75 nearest neighbors. For each projection technique, data for quicksort and bubble sort was combined, to obtain a shared embedding space. Duplicates were not removed prior to the embedding. For t -SNE and UMAP, the duplicate sorted arrays form a pronounced cluster, and the shared intermediate points are more salient. All plots were rotated such that the sorted end states are located to the right.

Figure 2 shows the sorting trajectories of all permutations of the list (1, 2, 3, 4, 5, 6) for bubble sort and quicksort, respectively. It shows results for projecting the states by means of t -SNE, UMAP, and Isomap. We used the state space representation and distance metric from the second bullet point in Section 3.1. To ensure comparability between the sorting algorithms, the results of bubble sort and quicksort were projected together into a shared embedding space—using one of the three dimensionality reduction techniques. We optimized the hyperparameters of each technique to obtain visually appealing results. Regardless of the embedding routine, the visualizations for bubble sort (Figure 2 (a–c)) exhibit long and winding trajectory bundles. Many different sorting trajectories need to go through the same few states before finally ending up in the sorted end state. For quicksort (Figure 2 (d–f)), the paths from the initial states to the sorted state are generally shorter, and do not overlap as much as in the case of bubble sort. This reflects the fact that, on average, quicksort only passes 3.5 intermediate states from start to finish, while bubble sort takes 7.5 steps for the given

lists of length 6. Furthermore, bubble sort is limited to simple swapping actions, which forces many sorting trajectories to take similar paths through the state space.

For all three embedding techniques, we did not remove duplicates prior to the embedding. For Isomap, duplicates in the input list do not make a difference, as equal high-dimensional points are mapped to equal two-dimensional points. For t -SNE and UMAP, however, high-dimensional duplicates are embedded as clusters in two dimensions. This behavior of t -SNE and UMAP is especially relevant for the cluster of sorted end states near the right of the plots in Figure 2 (a), (b), (d), and (e). The clusters make the trajectory bundles thicker and more easily traceable.

One insight from the comparison in Figure 2 is that, with the right parameter choice, t -SNE and UMAP can yield very similar plots. This is the case, when the perplexity parameter of t -SNE is chosen high enough for some global structure to be preserved. A typical argument in favor of UMAP is that t -SNE becomes inefficient for high perplexity values. However, this depends strongly on the size of the projected dataset, and on the chosen hyperparameters. For our guiding example we projected sorting trajectories for 720 different initial states, resulting in 8,640 non-unique states (i.e., including duplicates) in total. With the implementations we used (see Section 3.5), t -SNE with perplexity 100 was actually slightly faster than UMAP with 25 nearest neighbors. However, for larger datasets, higher dimensionality, or different hyperparameters, UMAP may perform better.

It should be noted that the state space for the guiding example of sorting algorithms for lists of length 6 is small enough that all possible initial states can be tried easily, and the state space can thus be projected as a whole. For more complex problems such as those described in Section 4, the state spaces are much larger, rendering it impossible to project them as a whole. In these cases, only the subspace of actually visited states is projected.

3.3 Patterns in Multiple Trajectories

As already seen in the guiding example from Figure 2, when multiple trajectories are constructed together, several different patterns can emerge. Figure 3 (a–f) shows the patterns we identified for start, intermediate, or end points, depending on whether they are sparsely distributed over large regions of the embedding space, or cluster more densely.

Obviously, tightly packed start points can be observed when the visualized processes are constrained to start from the same or from very similar states. This would be the case, for instance, in games that always start from a fixed initial configuration. Likewise, many processes converge to the same or to similar end states. Examples of these processes are list sorting (see Figure 2), optimization routines that reach global optima, or solution paths of puzzles such as the Rubik’s cube. As explained above, we mostly chose to not remove duplicate entries in the states lists prior to the embedding, which—in case of t -SNE or UMAP—leads to a tightly packed cluster instead of a single point in the embedding space even for exactly equal states.

Sparse clouds of start points in the embedding space typically come from randomly distributed initial states. Certain optimization algorithms, for instance, start with randomly initialized states. In high-dimensional space, the Euclidean distances between any two random states tend to be similar, with a variance limit of only $7/120$ [56]. Most nonlinear dimensionality reduction techniques based on distances in high-dimensional space tend to spread out many similarly spaced high-dimensional points onto a disk in the embedding space. This way, also sparse clouds of end points can emerge, if the visualized processes can terminate at many different, but similarly distant end states. The list sorting example from Figure 2 is difficult to categorize in terms of patterns of start points, since due to the small state space, all possible states were used as start points.

Perhaps the most interesting pattern among those described in Figure 3 (a–f) is the densely packed cluster of intermediate points of multiple trajectories through the embedding space (b). This pattern gives rise to *trajectory bundles*—groups of trajectories that share multiple consecutive clusters

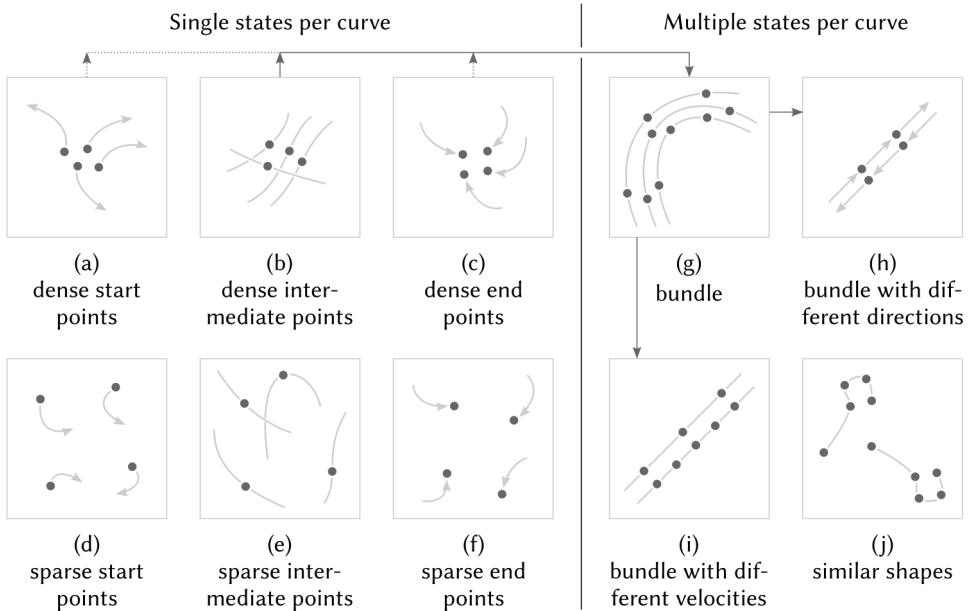


Fig. 3. Possible patterns emerging from multiple trajectories. The different kinds of points— start, intermediate, or end points—of several trajectories can be sparsely distributed over large regions of the embedding space, or more densely packed (a–f). Several consecutive intermediate point clusters (possibly together with start and/or end point clusters) lead to trajectory bundles (g). Trajectory bundles can differ in terms of direction (h), and/or state space velocity (i). The trajectories can also have similar shapes while populating entirely different regions of the embedding space (j).

of intermediate points. Trajectory bundles also play an important role in the guiding example in Figure 2, as their appearance is the main difference between the two sorting algorithms. In trajectory data mining, such bundles and similar structures have been described as flocks, convoys, swarms, or gatherings [62].

Figure 3 (g) shows how a trajectory bundle results from consecutive clusters of intermediate states (possibly also involving clusters of start and/or end states). It also shows that the trajectories within a bundle can differ in terms of direction (h) and/or velocity (i). However, interpreting the velocity is not straightforward. As explained in Section 3.1, the timestamps (if present) are not used for the projection of states—only for joining points to form trajectories. This means that two points close to each other in the embedding space do not necessarily need to be close in a temporal sense. A direct connection between two points means that the states they represent were visited consecutively, but the viewer might still not know about the “sampling rate”, i. e., the actual time between two states. In our applications, we deal with indexed states that often do not have a timestamp at all.

State space velocity can thus be interpreted in the sense of how many state changes are undergone between two non-consecutive points. Consider two trajectories, $a = \{a_1, \dots, a_n\}$ and $b = \{b_1, \dots, b_m\}$, that have two shared intermediate point clusters X and Y . Consider further that some $a_i \in X$ and $a_{i+1} \in Y$, which means that a progresses directly from X to Y . If now some $b_j \in X$ and $b_{j+2} \in Y$, but b_{j+1} lies somewhere between X and Y , then b has a *lower* state space velocity near state j than a has at i , because b needs more intermediate steps to traverse from X to Y . Such

a scenario is depicted in Figure 3 (i). A meaningful comparison of state space velocities is only possible when two trajectories share at least two intermediate point clusters.

Another pattern that can emerge from plotting multiple trajectories together is shown in Figure 3 (j). Two or more trajectories can have similar overall shapes, but lie in completely different regions of the embedding space. In case of nonlinear embedding techniques, such as *t*-SNE or UMAP, such patterns must be interpreted with care. The actual transformation from the high-dimensional manifold to the low-dimensional one may be considerably different for two separate state space regions. The only true insight gained from such patterns is that none of the states are similar across different trajectories. When the shape of many, well-separated trajectories is very similar (as will be the case in the neural network application discussed in Section 4.3), then a certain similarity of paths in the high-dimensional space—and thus a similar behavior of the real-world processes—can be assumed.

3.4 Visual Encoding and Interaction

Like Bach et al. [4], we use Bézier interpolation for connecting projected states to form trajectories. The improved readability compared to straight lines is especially important in our case, as we always display multiple trajectories. Depending on the application domain, the trajectories' hues in our visualizations encode categorical metadata attributes, and/or the brightness encodes the state index. To convey additional information, individual points can be represented with differently shaped markers associated with further metadata. Interaction can be used to extract additional information for individual or multiple states. This additional information is shown in a detail view. We will later explain the exact visual encoding of the trajectories, as well as the design of the detail view, for each example application separately.

3.5 Implementation

We used Python to prepare the datasets for the visualization. Details about particular packages used for data generation are listed separately within each application section (Sections 4.1, 4.2, and 4.3). For dimensionality reduction by *t*-SNE, we used either the scikit-learn [43] implementation, or the openTSNE implementation [46], the latter of which is preferable in terms of performance and reproducibility (see discussion in Section 5.1). We chose hyperparameters experimentally and list them with each example application. For Isomap we used the scikit-learn implementation, and for UMAP we used the official Python implementation of by McInnes [40]. The static visualizations were created in Python using matplotlib [28]. In a first prototype implementation, which is described in our previous workshop paper [51], we used TypeScript and D3.js [6] to render SVGs. This version of the prototype suffered from performance issues when many trajectories (≥ 50) were plotted. In our current implementation we use the three.js framework (<https://threejs.org>) and WebGL rendering for improved performance. This makes it possible to visualize hundreds of trajectories without any performance issues. The updated prototype is deployed at <https://jku-icg.github.io/projection-path-explorer>.

4 APPLICATIONS

4.1 Rubik's Cube Solution Algorithms

Rubik's Cube is a famous puzzle toy devised in 1974 by the Hungarian inventor and professor of architecture Ernő Rubik. With 350 million cubes sold around the world by January 2009, it is the world's top-selling puzzle game [1]. The classic version of Rubik's Cube has six faces, with each face being made up by a 3×3 grid of colored facets. These facets are the faces of smaller cubes, the so-called cubies. The cube consists of 26 such cubies: 8 corner cubies with three faces each, 12 edge

cubies with two faces each, and 6 center cubies with one facet each. The 27th cubie at the center of the cube is replaced by a mechanism that enables rotation of one 9-cubie slice of the cube at a time. For a standard Rubik's Cube, or any $n \times n \times n$ cube with odd n , the relative positions of the center cubies cannot change. The color of the center facet of one cube face is thus assigned to the whole face, and the cube is considered solved when each facet is correctly positioned on its color's face. Otherwise, the cube is said to be in a scrambled state.

Rubik's Cube is commonly known to be almost impossible to solve if no specific solution strategy or algorithm is applied. The closer a cube is to being solved and the more cubies are in the correct position, the more likely it is that any rotation with the intention of solving another part of the cube will scramble already correctly placed cubies. Therefore, precisely considered sequences of rotations need to be applied, which ensure that only specific cubies are moved to their intended destinations. Many solution strategies for Rubik's Cube have been developed. They differ in complexity and speed, depending on the amount of special patterns and conditions that are detected and utilized during the solving process. Generally, the faster a solution algorithm is and the fewer rotations are needed, the more sub-algorithms need to be learned and applied under the correct conditions. The classic beginners' method is highly inefficient but has only few sub-algorithms to be memorized. More advanced methods, such as Fridrich's CFOP method [17] or the Petrus method [44], are harder to learn but usually require significantly fewer moves. Generally, solution algorithms often use checkpoints: special points in the state space of the cube (e. g., having the yellow cross on the yellow side). This state space, in which the solution algorithms act, is high-dimensional and encompasses more than 4.3×10^{19} unique states.

4.1.1 Related work. Detailed information on a number of different Rubik's Cube solution algorithms has been compiled in several Wikis and Internet forums [16, 38]. AlgExplorer [54], published on such an online forum in 2017, is a command-line tool for exploring the algorithm/solution space based on an extensive record of Rubik's Cube solutions [30]. Scientific papers on Rubik's Cube have typically been concerned with finding optimal solutions. Kunkle et al., for instance, used out-of-core parallel computing and properties of the cube's permutation group to find a lower bound of 26 moves [32]. However, to our knowledge, no attempts at visualizing different solution strategies have been published.

4.1.2 State Space Representation. The first step of visualizing the solution pathways is transforming the cube states into numerical representations for further processing. We based the encoding of the cube state on the data structure underlying a Python Rubik's cube API [36], which we also used for calculating the solutions. Each face of the cube is represented by a 3×3 matrix with one entry for each facet. For the entries representing the facet colors we chose a one-hot encoding, i. e., (0,0,0,0,0,1) for red, (0,0,0,0,1,0) for green etc. This encoding facilitates the definition of meaningful distance metrics for the dimensionality reduction. The resulting $6 \times (3 \times 3) \times 6$ tensor was flattened, yielding a feature vector of length 324 for a single state.

Similarity in the original feature space is defined via a distance metric. We tried different metrics and ultimately chose the Euclidean distance. Euclidean distance in the high-dimensional state space does not take into account the number of operations (i. e., rotations of cube slices) which is necessary to go from one state to the next. Instead, we argue that applying the Euclidean distance to our choice of feature vectors yields a representation that is more in line with the intuitive judgment of how scrambled the cube is. In fact, for a one-hot encoding, the Euclidean distance is equal to the square root of the Hamming distance. The Euclidean distance thus corresponds to a "naive edit distance", that measures wrongly colored cube facets, but not the number of moves required to fix them.

4.1.3 Implementation and Visualization Details. The solutions were calculated from random initial states. Using a Python Rubik’s cube API [36], the initial states were generated by performing a set of random rotations on an initially solved cube. This ensured that only physically possible cube states were used. We added a new solution algorithm as well as options for data export to the API. For each state, we export the high-dimensional encoding as well as whether that state is a checkpoint of the used algorithm. Finally, we projected the high-dimensional cube states using t -SNE. For the 200 solution trajectories we used a learning rate of 100 and a perplexity of 50. For the plots with only 2 trajectories we used a perplexity of 20.

The trajectories for different solution algorithms are visually encoded by hue. Each state of a cube along its trajectory is displayed by a marker. We visualize the random origins as crosses, checkpoints as squares, and the solved states as stars, respectively. The square markers for different algorithm are slightly rotated, to make them distinguishable from one another when points are close together in the projected state space. Disk markers for intermediate states between checkpoints can be displayed on demand. The markers’ brightness encodes the progression through the solution trajectory, with bright colors corresponding to early states.

For each marker, a mouse-over action reveals a detailed view of the cube state, showing the colored facets of the unfolded cube. Multiple state markers can be selected using rectangular brushing. Selecting multiple states updates an additional detail view that features a similarity encoding: only those cube facets that have the same colors across all selected states are shown as full-sized, colored squares. For each remaining, non-constant facet, the color values are counted across all selected states. Each facet is colored according to the color with the highest number of counts, i. e., the most prevalent color for that facet. The non-constant facets are additionally shrunk and made transparent, with both the facet area and the alpha value being proportional to the count of the most prevalent color. This encoding ensures that constant facets across multiple states can be quickly identified, while information about the non-constant facets is preserved. An example of this similarity encoding can be seen in Figure 5.

A deployed version of our prototype implementation with pre-selected Rubik’s cube solution data can be accessed at <https://jku-icg.github.io/projection-path-explorer/?set=rubik>.

4.1.4 Results and Discussion. Figure 1 shows the projected solution trajectories for 100 randomly chosen initial cube states, both for the beginner’s method and the more advanced Fridrich’s method. Clearly, projecting the cube states with t -SNE leads to the formation of different clusters. Most prominently, later checkpoints form dense clusters close to the final solution (see (3) in Figure 1). Earlier checkpoints with fewer correctly positioned cube facets are much more spread out. These checkpoints share a wide, sparse region with the randomly selected initial states (1). In later stages along the solution paths, intermediate states tend to form clusters as well, which leads to bundles of parallel trajectories between checkpoints (2).

Figure 4 shows solution trajectories for the beginner’s method and Fridrich’s method applied to the same initial state (1). Our choice of color-mixing and the use of opacity reveal that the solution trajectories overlap completely up to the second checkpoint (2). Surprisingly, this almost perfect overlap was the case even though we used t -SNE (perplexity 20) for the embedding without removing duplicates first.

As the visualization, upon user demand, provides detailed views of unfolded cubes for all intermediate states, it can be seen that already two layers of the cube are fully solved at this point. We found this behavior to be general, i. e., independent of the initial state. Afterwards, the more optimized Fridrich method makes use of a large amount of different sub-algorithms. This avoids additional lengthy sequences of rotations close to the final solution. For the beginner’s method, these rotations show up as characteristic coils (3).

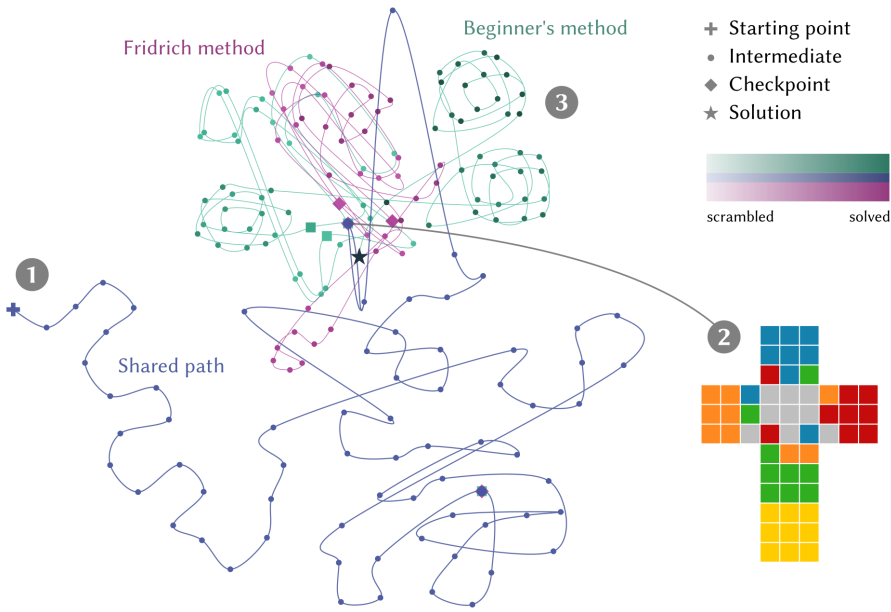


Fig. 4. Projected solution trajectories of the same initial state (1) solved with the beginner’s method and Fridrich’s method, respectively. The algorithms share the same path up to the second checkpoint (2), at which two layers of the cube are already fully solved. Near the end, the beginner’s method requires additional rotations, while Fridrich’s method approaches the solution much faster.

When projecting more cube solutions, the differences between the strategies due to the use of sub-algorithms become even more apparent (see Figure 1). Our visualization shows large bundles of trajectories as a result of clusters of similar intermediate points. Up to a certain point, these bundles appear similar for the two different techniques (2).

Selection of multiple states via brushing can help understand the origin of state clusters and trajectory bundles. As an example, we will look at one state cluster along the trajectory bundle in the upper right hand side of Figure 1. The similarity encoding for the cluster is shown in Figure 5 (b), along with the standard detail view for an individual state in the cluster (a). The similarity encoding reveals that about 70 percent of facets are equally colored across the states in the cluster. This particular cluster of intermediate points has a clearly defined sub-cluster, with four more white facets shared across all its states, as seen in Figure 5 (c). Also this more fine-grained analysis is made possible by multiple selection and the similarity encoding.

Further along the solution paths, the beginner’s method’s inefficient approach to correctly positioning the final cubies gives rise to a large cluster of many “avoidable” intermediate steps (see (4) in the left part of Figure 1). In case of Fridrich’s method, many fewer steps are required during the final stages of solving the cube, leading to a much smaller and less populated cluster of intermediate points (see (4) in the right part of Figure 1).

Thus, the scalability of our visualization approach to hundreds of cubes allows us to reliably detect differences between the beginner’s method and Fridrich’s method. Furthermore, the detail views for single and multiple state selections help users understand the structure of the embedding space. Thereby, these views clarify why patterns such as state clusters and trajectory bundles emerge.

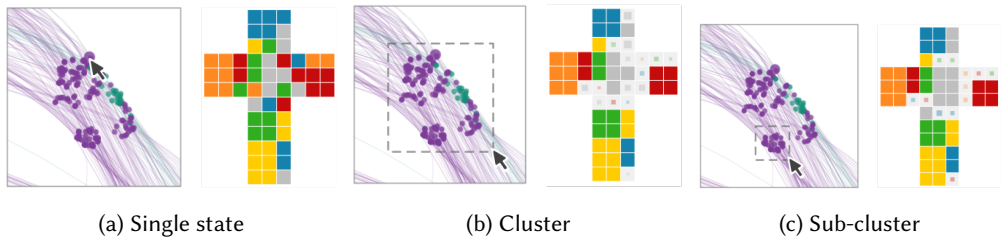


Fig. 5. Analysis of clusters and sub-clusters along trajectory bundles. Selecting a single point of a state in a cluster of intermediate points reveals the corresponding cube in the standard detail view (a). Selecting the whole cluster via brushing updates the similarity detail view (b). About 70 percent of cube facets are the same across the whole cluster. Selecting only the small sub-cluster shows that four more facets are the same (white) inside this sub-cluster (c).

4.1.5 Physical Interactive Demonstrator. To tighten the connection between our visualization approach and real-world actions and decisions made by users, we built a physical interactive demonstrator. The setup is shown schematically in Figure 6. It consists of a special Rubik’s cube with sensors and Bluetooth connectivity (Giiker Supercube, <http://www.giiker.cn>), a Lego Mindstorm robot (MindCub3r [19]), and a display showing an adapted version of the interactive Rubik’s cube visualization. While the user tries to solve the cube, rotations are immediately reflected in the visualization. The trail of previous cube states, as well as the current one, are shown in the embedded state space of several hundreds of reference solution trajectories of random initial cubes. Since the current cube state may not have been part of this initial set of calculated solutions, out-of-sample extension must be used. We implemented a parametric, real-time out-of-sample extension, based on the work by Gisbrecht et al. [20]. Along with the reference trajectories and the trajectory of movements performed so far, also the future path necessary to arrive at the solution is displayed (for a selected solution algorithm). Upon each cube movement, the future path is updated, if it has been affected by the user’s decision. This serves as a highly salient visual feedback for the user, as “incorrect” movements may result in drastic changes of the computed future paths. To aid the users, the correct movements to stay on the right track are shown with a rendering of Rubik’s cube. If users decide to stop trying to solve the cube on their own, they can hand the cube over to a Lego Mindstorms robot that will continue the solution. Users can then simultaneously watch the real cube being solved, while the current cube state moves along the solution trajectory in the visualization. The demonstrator setup also includes a two-player mode, in which two players can race through the solution trajectories with two separate Bluetooth cubes. The setup will be mainly used to introduce prospective computer science students to the functioning of algorithms, interactive visualization, and projection techniques.

4.2 Chess Games

The game of chess has a compact set of rules. For each piece—king, queen, rook, bishop, knight, and pawn—only a limited set of movements are allowed. Nevertheless, chess is extremely rich in tactics and strategy. Players need to continuously evaluate the positions of the pieces on the board, and adapt their future moves accordingly. To strengthen their skills, players typically study records of games, often with annotations from experts.

A game of chess can be roughly divided into the three stages of opening, middlegame, and endgame. In the opening phase, players aim to develop their pieces (i. e., move them to strategically relevant positions), take control of the center of the board, ensure safety of their king, and structure

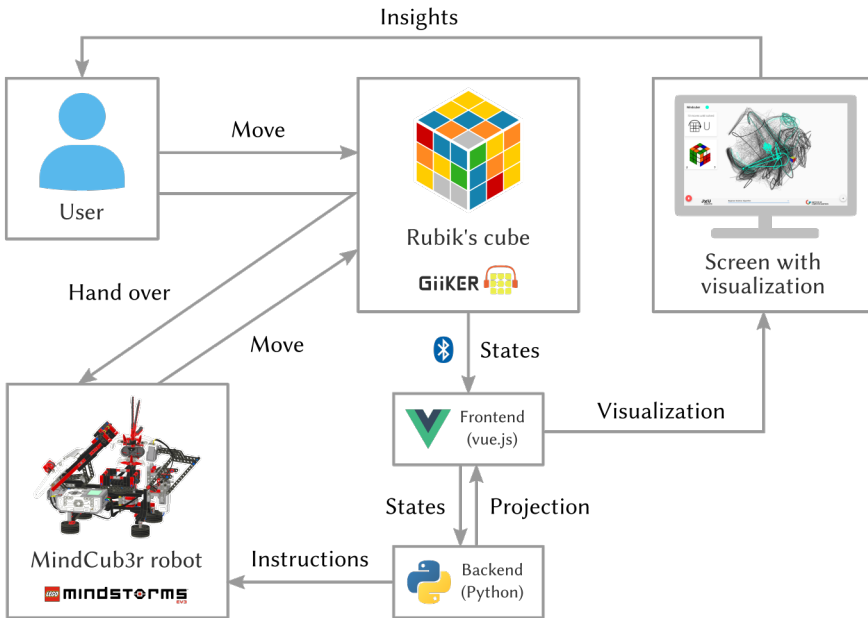


Fig. 6. Schematic of the Rubik's cube physical demonstrator setup. Users can solve a Rubik's cube, which transmits its states to a vue.js-powered web application via Bluetooth. The projected cube states are calculated in real time using out-of-sample extension implemented in Python. The projection of the current state and the previous trajectory are visualized on a screen. Users can hand off the unsolved cube to a Lego Mindstorms robot, which receives its instructions from the Python backend, and automatically solves the cube.

their pawns. The middlegame mostly depends on the openings chosen by the two players. It is typically the phase where most captures occur, often as results from so-called combinations. Finally, the endgame is the phase of the game, in which only few pieces remain on the board. Important goals in this stage are promotion of pawns, strategic positioning of the king, and forcing the opponent to make certain moves—a situation called *zugzwang*. Players win either by checkmate or resignation of their opponents. A game can also end in a draw for a number of reasons, including agreement or a stalemate.

Using our visualization approach, we explore possible similarities between how games proceed through these phases. We apply our visualization approach to chess by viewing the chessboard as a state space, with each configuration of pieces position corresponding to one possible state. Each of the players' moves causes the game to proceed from one state to the next. The number of reachable positions has been estimated to lie between 2×10^{43} and 1.8×10^{46} [10].

4.2.1 Related work. Classic tools for computer-aided studying of chess games, such as Fritz 16 [18], typically feature a simple chessboard visualization of one game state at a time. Along with the chessboard, usually a list of the moves of the game is shown. Additionally, possible alternative moves and their immediate impact may be presented to the users.

Instead of focusing on single snapshots of the game, Lu et al. visualize the evolution of entire games [37]. They introduce the evolution graph, a decision tree visualization that combines the actual moves performed by the players with alternative moves calculated by AI. Along with the moves, advantage scores for each player are given.

Table 2. State space representations for board states before and after different kinds of moves on a simplified 2×2 chessboard with two different pieces. The pieces are encoded as $\blacksquare = (0, 1, 0)$ and $\triangle = (0, 0, 1)$, and empty fields as $(0, 0, 0)$. For simplicity of the representation, castling and promotion are performed across colors. The listed distances are Euclidean distances with respect to the initial state given in the first row.

Movement	Board	Tensor	Vector	Distance
None (initial)		$\begin{pmatrix} (0, 0, 0) & (0, 0, 1) \\ (0, 1, 0) & (0, 0, 0) \end{pmatrix}$	$(0, 0, 0, 0, 0, 1, 0, 1, 0, 0, 0, 0)$	0
Simple		$\begin{pmatrix} (0, 1, 0) & (0, 0, 1) \\ (0, 0, 0) & (0, 0, 0) \end{pmatrix}$	$(0, 1, 0, 0, 0, 1, 0, 0, 0, 0, 0, 0)$	$\sqrt{2}$
Capture		$\begin{pmatrix} (0, 0, 0) & (0, 1, 0) \\ (0, 0, 0) & (0, 0, 0) \end{pmatrix}$	$(0, 0, 0, 0, 1, 0, 0, 0, 0, 0, 0, 0)$	$\sqrt{3}$
Castling		$\begin{pmatrix} (0, 0, 0) & (0, 1, 0) \\ (0, 0, 1) & (0, 0, 0) \end{pmatrix}$	$(0, 0, 0, 0, 1, 0, 0, 0, 1, 0, 0, 0)$	2
Promotion		$\begin{pmatrix} (0, 0, 1) & (0, 0, 1) \\ (0, 0, 0) & (0, 0, 0) \end{pmatrix}$	$(0, 0, 1, 0, 0, 1, 0, 0, 0, 0, 0, 0)$	$\sqrt{2}$

Thinking Machine 6 [61] is another approach related to our work. It visualizes potential moves considered by an AI as trajectories on the chess board. The brightness of the trajectories encodes how advantageous the outcome of the sequence of movements will be. Additionally, the importance of each piece is visualized by a rippling animation of the background.

Instead of visualizing potential movements for single games, our approach focuses on revealing patterns emerging from showing the actual movements made in many games together.

4.2.2 State Space Representation. For representing the possible configurations of pieces numerically, we started by viewing the chessboard as an 8×8 matrix. Each field can be populated by one of 12 different pieces (six different pieces each for black and white), or it can be empty. We thus represented the state of one field by a one-hot code of length 13, resulting in a $8 \times 8 \times 13$ tensor encoding the full board state. This tensor was flattened, yielding a vector of length 832. As in the case of the Rubik's cube visualization, we chose to use the Euclidean distance. The results of this choice for the different kinds of moves are detailed in Table 2. Using this encoding and the Euclidean distance has the consequence that moving a bishop diagonally by 1 or 4 fields, for instance, does not result in different state space distances (as long as no captures occur). Both resulting states have a distance of $\sqrt{2}$ to the previous state, and the same is true for all simple movements, as well as promotions (see first and last row of Table 2). The states resulting from castling, on the other hand, have distance 2 to the previous state, and captures result in a state space distance of $\sqrt{3}$. The type of move (capture, castling, promotion, etc.) leading to each state can additionally be regarded as metadata.

4.2.3 Implementation and Visualization Details. The chess game records used for the visualizations in this chapter are freely available at KingBase [22] in the Portable Game Notation (PGN) format.

We parsed the PGN files using the chess module of the `pgn2gif` Python package [55]. The resulting sequences of chessboard states were encoded as described above.

The trajectories for different opening moves are visually encoded by hue. Each intermediate state is represented by a marker. We visualize the initial state (standard chess setup) as crosses, and the final states of the games as stars. For each marker, a mouse-over action reveals a view of the chessboard. Similar to the Rubik's cube application, selecting multiple states by rectangular brushing updates a similarity detail view. Fields with varying chess pieces across the selected states show only the most prevalent piece. The piece is made transparent, with an alpha value proportional to the counts for the most prevalent piece on that field across all selected states.

A deployed version of our prototype implementation with pre-selected chess game data can be accessed at <https://jku-icg.github.io/projection-path-explorer/?set=chess>.

4.2.4 Results and Discussion. Figure 7 shows decision trajectories for 200 randomly selected chess games between players with Elo scores greater than 2,000. The games are colored depending on the first move by white, which was either the Queen's Pawn Game (d3) or the Zukertort Opening (Nf3). Next to the King's Pawn Game, these two moves are among the three most common openings.

As each game starts from the same board state, a dense cluster of initial states is visible in Figure 7 (a). From this cluster, two trajectory bundles emerge—one for each of the two openings. Subsequently, the bundle resulting from the Queen's Pawn Game splits up into one narrow bundle down and one wide bundle going up. These bundles reflect the first move performed by black (f5 and e6, respectively). A similar splitting can be observed for the games starting with the Zukertort opening. Even several states later, still only few trajectory bundles are visible in the lower right and right part of Figure 7. This makes sense as certain for each opening there are only a few established reactions.

The later intermediate states, roughly between the opening phases and the middlegames, form three particular structures. Two clusters, seen in Figure 7 (b) and (c), are collections of game states resulting from earlier castling moves. The transparency encoding in the interactive detail view revealed that the main difference between these two clusters is the position of two black pawns. In the lower cluster (b), two of the black pawns are placed on c6 and d5. In the upper cluster (c), they are instead placed on c7 and d6. Interestingly, games for the two different openings are not represented equally in each cluster. The Queen's Pawn Game seems to be overrepresented in the cluster related to black pawn positions c6 and d5, while the Zukertort Opening is slightly overrepresented among games in the cluster related to black pawn positions c7 and d6.

Finally, at some point the trajectories tend to make large jumps to a distinct region in the state space, where each game culminates in a sequence of densely threaded intermediate states. These dense sequences before the endstates are representations of endgames. Those endgames in which only few pieces remain converge in a similar region of the state space, as seen in Figure 7 (e). The final states of all other games form the pattern described in Figure 3 (f).

Considering the simple encoding of the chessboard that we chose as our state space representation, it is surprising to see actual gameplay patterns emerge from the embedded trajectories. These patterns are only possible when many trajectories are constructed together. Furthermore, the application of decision trajectories to chess games showed that interactive exploration is vital for relating visual patterns to the real-world meaning. In future work, we plan to cooperate with a professional chess player to explore how exactly the patterns correlate with strategic decisions made by players.

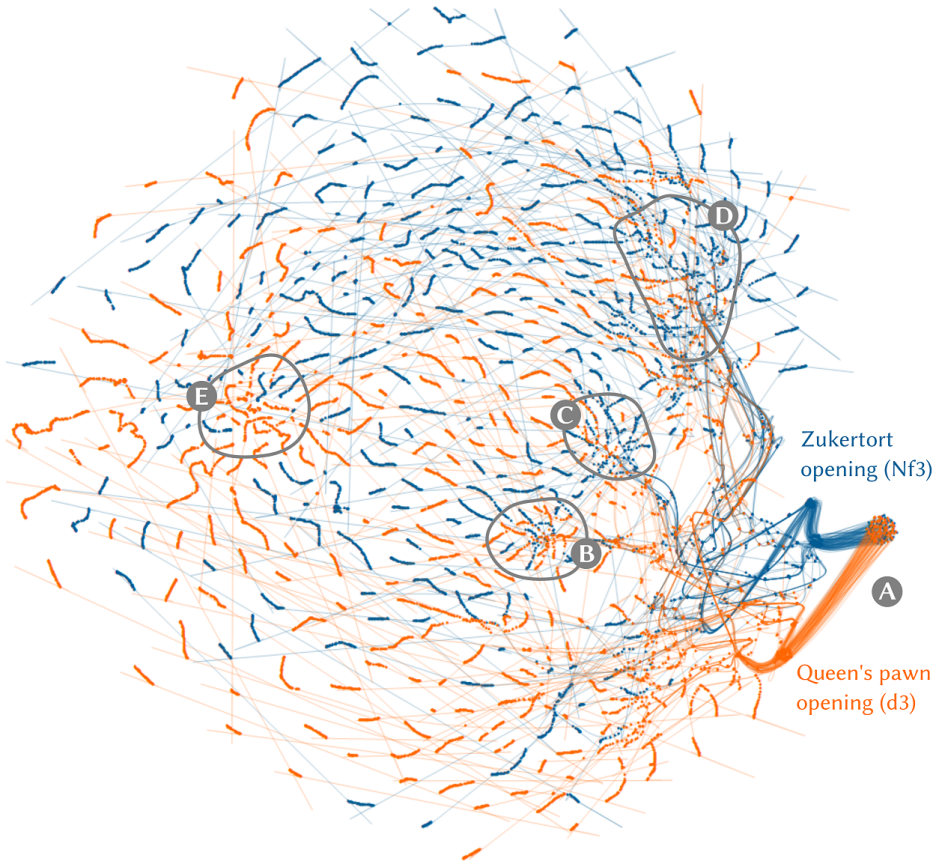


Fig. 7. Visualization of 200 chess game trajectories for two different openings, Queen's Pawn Game (d3) and Zukertort Opening (Nf3), respectively. Several trajectory bundles emerge from the cluster of equal initial states (a). Two smaller clusters of intermediate game states are visible near the center of the plot. Both clusters consist of games states resulting from earlier castling moves. The lower cluster (b), has black pawns placed on c6 and d5. The upper cluster (c) has black pawns placed on c7 and d6, respectively. Game states resulting from a certain kind of pawn defense cluster towards the upper right side of the plot (d). Finally, endgames with only few pieces remaining form a more densely packed cluster (e), while other endgames are spread out evenly across the embedding space.

4.3 Neural Network Training

Deep neural networks are a class of powerful, nonlinear models that can learn complex representations of data. They have greatly improved the state of the art in a diverse range of application domains, including computer vision, speech recognition, drug discovery, and genomics [34]. However, deep neural networks are often highly overparametrized, and their learning behavior is difficult to interpret. It is usually not clear, how a certain choice of hyperparameters or a certain train/test split affect the final performance of the model. With the growing impact of deep learning on real/world decision-making, these difficulties have led to an increased demand for explainable

or interpretable models. One possible way of analyzing, understanding, and communicating the processes during deep learning is visualization [26].

The behavior of deep neural networks depends on many different aspects: training and test data, the network architecture, choice of optimization technique and hyperparameters, the actual learned weights, and the resulting activations for each input. Most of these aspects be visualized, and almost all of them—even architecture and training data—may change over the course of the training. As such, the training of neural networks can be viewed as sequential steps through a high-dimensional state space. Furthermore, developing well-functioning deep models is a highly incremental and iterative process, that requires model builders as well as model users to compare the behavior for many different experimental configurations. This combination of “temporality” and the need for comparative analysis makes training of neural networks a perfect candidate for a visualization using multiple embedded trajectories. In this section, we will show how groups of trajectories constructed from different state space representations can selectively uncover different aspects of the learning processes of an image classifier.

4.3.1 Related work. As stated above, visualizations in the context of deep learning are becoming increasingly popular [26]. Dimensionality reduction has been applied to visualize the representations learned by convolutional neural networks [3, 11], deep Q-networks [41], or deep belief networks [21, 42], among others. However, in most cases, only the projections for one time step are shown—usually after the learning has finished. Only few works combine dimensionality reduction techniques with the temporal progression of the training process. Rauber et al. visualized the inter-epoch evolution of neuron activations as trajectories in an embedding space [47]. Even more closely related to our work is a visualization used by Erhan et al. in their study of pre-training of neural networks [14]. They show learning trajectories through function space, which is one particular state space representation. We will show results for two other choices of representations, one of which will also motivate why Erhan et al. chose their function space representation.

4.3.2 State Space Representation. We chose two different state space representations: a representation of the weight space and a representation of the confusion matrix.

The *weight representation* corresponds directly to the weights learned by the network. For a given layer, we flatten the associated weight matrix to a single vector. After each training epoch, the weights are updated and a new weight vector can be obtained. The length of the vectors, and thus the dimensionality of the state space for this representation, depends on the network architecture. It is equal to the number of units in that layer, times the number of units in the previous layer. We use the Euclidean distance as a metric for comparing weight vectors.

The *confusion matrix representations* is more closely connected to network performance. At each epoch, we let the network classify all test instances, and construct the resulting confusion matrix. Each cell (i, j) in the confusion matrix lists the number of instances with ground truth class label i and predicted class label j . This state space representation is only suitable for supervised classification problems. The length of the flat confusion vector is k^2 , where k is the number of different classes. We experimented with using the Euclidean distance as well as the cosine distance for comparing confusion states, but found that the resulting plots look very similar for both metrics. Here, we only show trajectories constructed using the Euclidean distance.

4.3.3 Implementation and Visualization Details. We used PyTorch (<https://pytorch.org/>) to train a simple neural network to classify MNIST [33] images. To reduce the number of weights in the hidden layer, we decided to reduce the dimensionality of the input data to 50 by means of PCA. We also chose 50 as the number of units in the hidden layer, resulting in 2,500 weights between the input and hidden layers. We used ReLU as activation function, stochastic gradient descent for

optimization, and cross entropy loss. We tried different learning rates between 0.01 and 1. In most of our experiments, we trained the networks for 20 epochs, and used the standard MNIST train/test split.

The visual encoding of the trajectories is similar to the previous two applications, with intermediate states encoded by point marks, and initial states encoded by crosses. For the static plots in this section, however, we treat final states like intermediate states (point mark). We chose this encoding since we stopped the training after a fixed number of epochs, which does not constitute a true end state of the training process.

For our experiments with different learning rates, we colored the trajectories categorically by learning rate. The detail view for single state selection is a visualization of the confusion matrix of the network at this state. The confusion matrices were evaluated for the MNIST test sets. Since all networks learned relatively fast, a naive visualization of the confusion matrix would look similar to a diagonal matrix already after the first epoch. To instead direct the users' attention to the errors, i.e., the off-diagonal values, we left the diagonal blank and adjusted the color scale accordingly. We recently used a similar approach in a visualization tool for comparing confusion matrices across time [24].

A deployed version of our prototype implementation with pre-selected learning trajectories can be accessed at <https://jku-icg.github.io/projection-path-explorer/?set=neural>.

4.3.4 Results and Discussion. For our first experiments, we wanted to see whether the notion of “learning speed” is conserved in the embedded trajectories for neural network training. To this end, we used several different learning rates, and initialized all networks with the same (randomly chosen) initial weights. The corresponding trajectories are shown in Figure 8, where the top plot (a) shows trajectories constructed from the weight space representation, while the bottom plot (b) shows trajectories constructed from the confusion matrix representation. Different learning rates are encoded by hue, and the values are listed in colored insets. In both plots, the equal initial states are represented by a cluster of crosses, a typical pattern described in Figure 3 (a). It can be seen that the dimensionality reduction technique—in this case t -SNE with perplexity 40—does not always behave the same with regards to clustering equal states. In the weight space representation, the initial states are slightly spread apart, while in the confusion embedding space, they are extremely tightly packed. The overall trend, however, is the same for both representations. As expected, low learning rates lead to smaller changes in the networks' weights, as well as in their classification behavior. Slow progression through the state space is reflected in the trajectories by high density of intermediate states, as shown schematically in Figure 3 (i). This is also the case near the end of the training, when the optimization starts to converge.

Figure 8 (a) shows that, in the weight space, the trajectories for learning rates between 0.01, 0.2 all move in the same direction. The trajectories for 0.5 and 1 move into a different region of the embedded state space. However, from the weight space representation, no insight about performance can be gained. Even from the confusion embedding, without any additional tricks, only insight about similarity of performances can be gained. Absolute performance, i. e., overall accuracy, cannot readily be determined from the embedding. To fix this shortcoming, we added additional structure to the confusion embedding space, by augmenting it with the projected confusion matrix for perfect classification. This single state was added to all other confusion matrices before performing the dimensionality reduction. It is shown as a gray star in Figure 8 (b), and denoted by $\text{diag}(x_1, \dots, x_k)$, since it is a diagonal matrix with the class distribution along its main diagonal. In this augmented state space it should be possible to interpret intermediate state in terms of network performance, by assessing the distance to the added diagonal matrix. In fact, calculating the classification accuracy for all learning rates after 20 epochs gives slightly lower values for 0.5 and 1. A learning rate

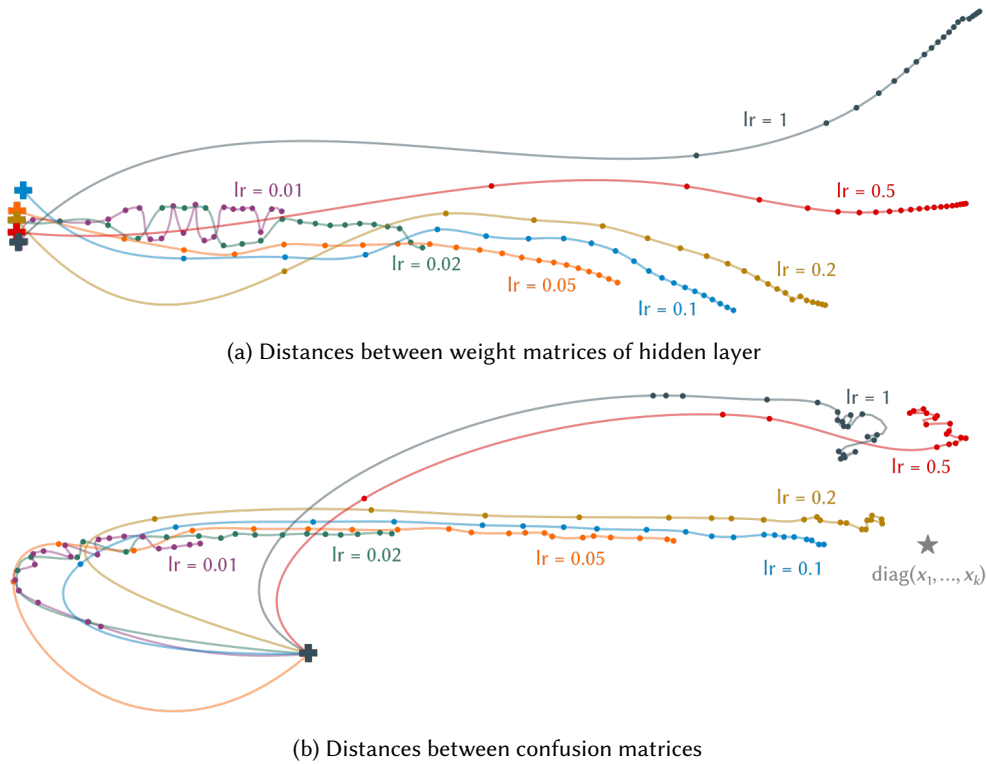


Fig. 8. Learning process of neural networks trained with different learning rates using a dimensionality reduced (PCA) version of the MNIST images as training data. The initialization was the same for all networks. Trajectories projected by t -SNE from two different state space representations are shown: (a) based on the weight matrices of the hidden layer; and (b) on the confusion matrices for the test dataset. Both representations resulted in groups of trajectories with similar patterns. The state space of the confusion matrix representation can be made interpretable by augmenting it with the confusion matrix of perfect classification, denoted by $\text{diag}(x_1, \dots, x_k)$.

of 0.2 yielded the best classifier in terms of accuracy, as would be expected from the embedded trajectories.

From Figure 8, it looks as if the two representations—based on weights or confusion—carry mostly the same information. However, this is generally not the case! Figure 9 shows 30 networks trained on MNIST data, all with the same learning rate (chosen as 0.2 based on the insight from the previous example) and the same architecture. The only difference between the 30 networks is the random initialization of the weights. In the weight space embedding, all networks quickly move towards their own region, where they converge in a chain of densely packed intermediate states. The reason for no two networks being similar in Figure 9 (a) is the fact that many different weight configurations can result the exact same mapping function from inputs to outputs. This phenomenon is known as weight space symmetries. To address this issue, Erhan et al. [14] chose a function space representation instead. We chose a confusion matrix representation, which—as detailed above—in addition to revealing differences in the mapping functions also can be interpreted in terms of classification accuracy. In this embedding, shown in Figure 9 (b), it becomes clear that the networks are indeed much more similar with respect to their classification and learning behavior as

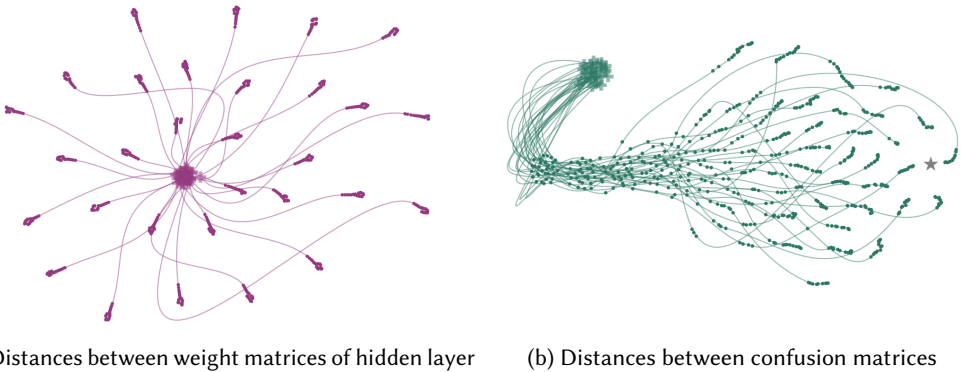


Fig. 9. Learning process of neural networks trained equal learning rates but different random initialization, using a dimensionality reduced (PCA) version of the MNIST images as training data. Trajectories embedded using t -SNE, based on two different state space representations, are shown: (a) based on the weight matrices of the hidden layer; and (b) on the confusion matrices for the test dataset. For the confusion matrix representation, the state space is augmented with the confusion matrix of perfect classification, which is denoted by the gray star.

one would expect from the weight space embedding. However, regardless of whether the function or the weight space representation is chosen, care must be taken in interpreting the distances in the trajectory visualizations. In Figure 9 (b), absolute distances between final confusion matrices for differently initialized weights are artificially “blown up” by the projection technique trying to conserve relative distances within the chains of very similar matrices near the end of each trajectory. Nevertheless, this example demonstrates the power of using different state space representations for showing different aspects of high-dimensional processes with embedded trajectories.

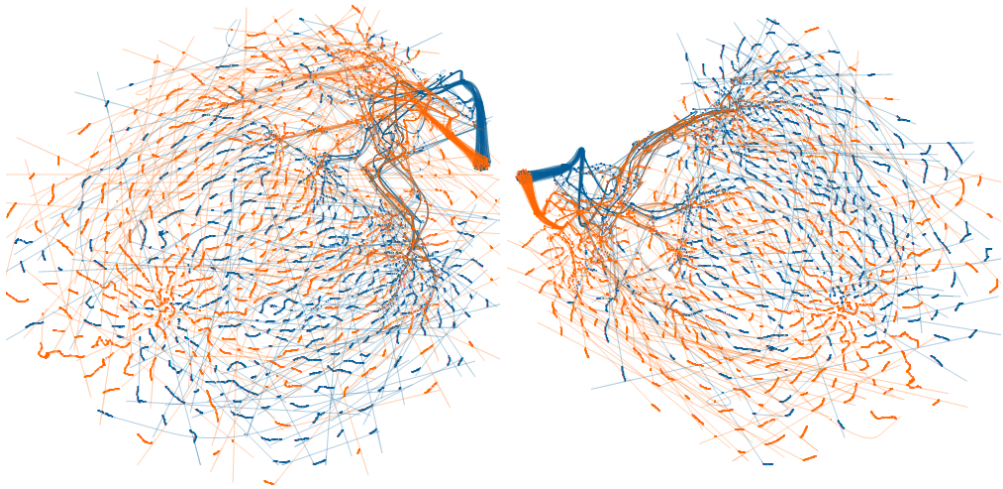
5 LIMITATIONS AND FUTURE DIRECTION

5.1 Limitations Related to Dimensionality Reduction

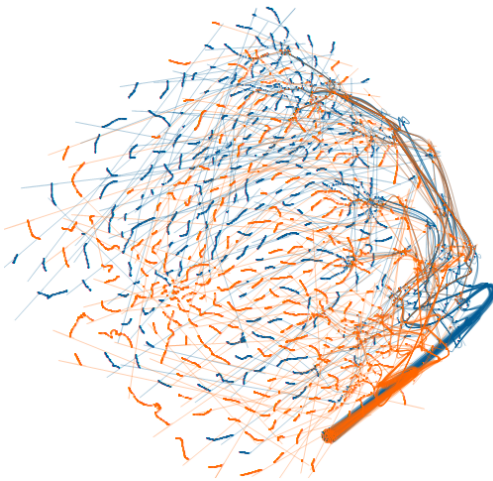
When high-dimensional states are represented in a two-dimensional embedding space, naturally not all original distance information can be preserved. Depending on the dimensionality reduction technique, several shortcomings are introduced.

Since the absolute position of points in the embedding space does not have a true meaning (at least in case of t -SNE and UMAP), interesting patterns may sometimes be placed at regions of the embedding space where they are hard to spot. In case of the comparison of Rubik’s cube solution algorithms, for instance, the two “handles” to the upper left and upper right of each plot in Figure 1 were not always placed at a region of the embedding space that allowed for assessing the similarities of the two algorithms. More problematically, all projection techniques may introduce pattern artifacts. These artificial patterns can only be distinguished from the real ones discussed in Section 3.3 by using interaction and a detail view that allows the user to inspect individual states.

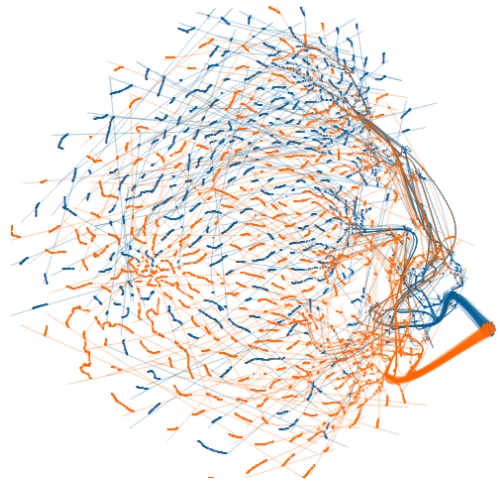
One way to make sure that patterns emerging from the trajectories are real, is to repeatedly run the embedding with different random initializations. Those patterns that are present regardless of random fluctuations, are unlikely to be artifacts. Figure 10 (a) shows two examples of randomly initialized t -SNE embeddings for the chess data from Figure 7. Once real patterns have been identified, certain tricks can be used to make the embedding less susceptible to random perturbations. In the t -SNE implementation that we used [46], random initialization of low dimensional positions



(a) Random initialization, perplexity 150



(b) PCA initialization, perplexity 50



(c) PCA initialization, perplexity 100

Fig. 10. Embeddings of chess games from Figure 7, re-run with random initialization and same perplexity (a), and with different perplexity values but fixed PCA initialization (b, c). The PCA initialization ensures similar global orientation. Several re-run embeddings with random initialization provide information about possible artifacts.

can be replaced by initialization with PCA results. As shown in Figure 10(c) and (d), this makes the global appearance of the embedding more stable, even when the perplexity parameter is changed.

Furthermore, the objective function of t -SNE, as opposed to that of UMAP, does not strictly penalize for two points with large high-dimensional distance to be embedded close together. This is one of the reasons why t -SNE typically cannot preserve global structure as well as UMAP. However, we found that local structure often seems to be more important than global structure for interpreting embedded trajectories. We assume that this is because the processes we visualized often featured

small, sequential steps rather than large jumps in the high-dimensional state space. Additionally, with the right choice of hyperparameters—perplexity in the case of t -SNE, and minimum distance and number of nearest neighbors in the case of UMAP—both techniques yield relatively similar plots.

Unfortunately, hyperparameter search for both t -SNE and UMAP is relatively slow, as both techniques are computationally expensive. This computational overhead makes it difficult to construct interactive visualizations with changeable hyperparameters. Instead, several embeddings need to be pre-computed if the user should be given a choice.

Even when multiple embeddings are pre-computed, the non-convex nature of the objective functions used in t -SNE and UMAP can still be problematic. If no pre-computed initialization is used, slight changes of the hyperparameters can result in vast visual differences. Thus, any sort of interaction allowing changes in the dimensionality reduction is challenging to implement.

Finally, the non-convex objective function of t -SNE and UMAP makes it impossible to add points to an existing embedding without completely changing the whole visualization. In the physical interactive Rubik's cube demonstrator we solved this problem by using out-of-sample extension [20]. However, with each new point added in this way to an existing embedding, the visualization becomes less accurate. Therefore, for out-of-sample extension to work well, as many different potential high-dimensional states as possible have to be included in the initial embedding.

5.2 Limitations Related to State Space Representations and Distance Metrics

Choosing a meaningful combination of state space representation and distance metric for the construction of decision trajectories can be challenging. As already hinted at in Section 4.1 about Rubik's cube solution strategies, it might not always be possible to find a state space representation that can accurately preserve the real-world notion of distances between states. For the Rubik's cube example, a combination of representation and metric would be ideal, if it puts two cube states at a distance of 1 if one state can be reached from the other in one single quarter-turn of a cube face. Even if such a representation existed, it would have to be based on finding the shortest path between two cube states in terms of rotations. An algorithm capable of solving Rubik's cube with the shortest possible sequence of moves has been termed God's Algorithm, and proving the lower bound of necessary moves alone took 35 CPU-years in 2010 [48]. To our best knowledge, there is still no efficient implementation for finding the shortest path between two arbitrary states. Therefore, the Rubik's cube visualization shows that it is sometimes necessary to use a simpler state space representation, and hope that the representation and metric preserve interesting features of the real-world processes.

Furthermore, for many applications certain symmetries could be exploited in the state space. In case of the Rubik's cube, many cubes are equivalent with regards to solutions involving, for instance, the yellow or green cross as a first checkpoint. Likewise, chessboard states could be seen as equivalent if white and black pieces are swapped. For chess, it could be argued that this symmetry is broken by the rule of white always performing the first moves. Still, reflection-symmetrical states could be regarded as equivalent. In case of Rubik's cube, we broke the symmetries consciously by forcing each cube to pass the same checkpoint (yellow cross)—essentially disregarding more efficient solutions involving different checkpoints.

For both the chess and the Rubik's cube visualizations, disregarding the symmetry still led to interpretable trajectory patterns. However, many applications could benefit from a state space representation and/or distance metric that takes symmetries into account.

5.3 Limitations Related to the Visual Encoding

In order to keep visualizations with hundreds of trajectories readable, interpolation between points is extremely important. Unfortunately, each interpolation technique may introduce artifacts such as overshooting splines. An example of such artifacts can be seen in Figure 7 close to the final chain of points for each game.

Additionally, not each interpolation technique is equally suited for adding points to trajectories on the fly. Newly added points may change the shapes of trajectories through many of the previous points severely. For the physical interactive Rubik's cube demonstrator, the ability to add points to existing trajectories on the fly is important for creating an immersive experience. To make this addition as unobtrusive as possible, we used cubic cardinal splines. This spline interpolation technique makes sure that adding a point alters only the trajectory through the last three intermediate points.

Even with a suitably chosen interpolation technique, trajectories through the embedded state space may cause visual clutter. We plan to experiment with edge bundling techniques to address this issue in future versions of our applications of decision trajectories.

5.4 Future Work

As stated in Section 4.2, we plan to examine the correlation between players' strategies and patterns in trajectories of chess games in more detail. To this end, we are currently initiating a cooperation with a professional chess player. We will then apply our visualization technique not only to chess games by human players, but also to games played by chess computer programs. Especially, it would be interesting to compare strategies used in classic chess computer programs with those learned by state-of-the-art reinforcement learning algorithms such as AlphaZero [50].

In light of potential future collaborations with domain experts, we plan to further improve the interactivity of our prototype. We are currently considering automatic pattern recognition based on clustering and trajectory data mining techniques [62]. Such automatically found patterns could be used to draw the user's attention to specific regions of the embedding space, possibly by using automatically created insets as demonstrated in a recent work by Lekschas et al. on pattern-driven navigation [35].

Currently we are working on a project about finding and understanding user actions in interactive visualizations. We plan to employ a similar, but less domain-specific approach as Brown et al. did in ModelSpace [8]. Our aim is to extract interaction data from provenance graphs of visualization applications and visualize the data as multiple trajectories through the same embedding space. This embedding space will be based on a representation of the visualization's properties that are changed by the users' interactions. We hypothesize that patterns emerging from multiple projected interaction trajectories can give insight about the users' sensemaking processes.

6 CONCLUSIONS

In this paper, we explored visual patterns in projected problem solution paths. This was possible by viewing the decisions—whether made by humans or resulting from the rules of an algorithm—as transitions between states in a high-dimensional representation space.

To reveal and explore the patterns, we projected multiple paths through the high-dimensional state space as trajectories in a shared, low-dimensional embedding space. We found this approach general enough to be applied in various application domains.

In the context of Rubik's cube, we related trajectory patterns to different traits of solution algorithms. We also presented a physical interactive demonstrator, which lets users perform moves

on a Rubik's cube with Bluetooth connectivity. In this demonstrator, our visualization approach gives immediate feedback about the decisions made by users.

In our visualization of chess games, we showed that interactive exploration of the trajectories allowed to correlate patterns in the projection to different tactics and board states. We plan to strengthen the connection between trajectories and chess strategies in a future collaboration with a professional chess player.

Finally, our application of embedded trajectories to neural network training showed the importance of expressive similarity metrics in the high-dimensional representation space. A comparison of weight similarity and confusion similarity proved that the interpretability of embedded trajectories depends strongly on these metrics.

For all our applications, we used the same interactive visualization prototype. This general prototype can be adapted easily to new domains, simply by defining new encodings for the detail view. In the future, we plan to adapt the prototype for visualizing user interactions in visual analytics applications.

We hope that our work will inspire future studies of projected decision trajectories in a variety of interesting application domains.

ACKNOWLEDGMENTS

This work was supported in part by the State of Upper Austria (FFG851460, Human-Interpretable Machine Learning) and the Austrian Science Fund (FWF P27975-NBL).

REFERENCES

- [1] William Lee Adams. 2009. The Rubik's Cube: A Puzzling Success. *Time Magazine*. <https://web.archive.org/web/20090201200141/http://www.time.com/time/magazine/article/0,9171,1874509,00.html>
- [2] Natalia Andrienko and Gennady Andrienko. 2013. Visual analytics of movement: An overview of methods, tools and procedures. *Information Visualization* 12, 1 (Jan. 2013), 3–24. <https://doi.org/10.1177/1473871612457601>
- [3] Mathieu Aubry and Bryan C. Russell. 2015. Understanding Deep Features with Computer-Generated Imagery. In *2015 IEEE International Conference on Computer Vision (ICCV)*. IEEE, Santiago, Chile, 2875–2883. <https://doi.org/10.1109/ICCV.2015.329>
- [4] Benjamin Bach, Conglei Shi, Nicolas Heulot, Tara Madhyastha, Tom Grabowski, and Pierre Dragicevic. 2016. Time curves: Folding time to visualize patterns of temporal evolution in data. *IEEE Transactions on Visualization and Computer Graphics* 22, 1 (2016), 559–568. http://ieeexplore.ieee.org/xpls/abs_all.jsp?arnumber=7192639
- [5] JÄirgen Bernard, Nils Wilhelm, and Maximilian Scherer. 2012. TimeSeriesPaths: Projection-Based Explorative Analysis of Multivariate Time Series Data. *Journal of WSCG* 20, 2 (2012), 97–106.
- [6] Michael Bostock, Vadim Ogievetsky, and Jeffrey Heer. 2011. D3: Data-Driven Documents. *IEEE Transactions on Visualization and Computer Graphics* 17, 12 (2011), 2301–2309. <https://doi.org/10.1109/TVCG.2011.185>
- [7] Hasan Alp Boz. 2019. *A Visual Multivariate Dynamic EgoCentric Network Exploration Tool*. Master's thesis. Sabanci University, Istanbul, Turkey.
- [8] Eli T Brown, Sriram Yarlagadda, Kristin A Cook, Alex Endert, and Remco Chang. 2018. ModelSpace: Visualizing the Trails of Data Models in Visual Analytics Systems. In *MLUI 2018: Machine Learning from User Interactions for Visualization and Analytics*. IEEE, Berlin, Germany, 11.
- [9] Eren Cakmak, Daniel Seebacher, Juri Buchmuller, and Daniel A. Keim. 2018. Time Series Projection to Highlight Trends and Outliers. In *2018 IEEE Conference on Visual Analytics Science and Technology (VAST)*. IEEE, Berlin, Germany, 104–105. <https://doi.org/10.1109/VAST.2018.8802502>
- [10] S. Chinchalkar. 1996. An Upper Bound for the Number of Reachable Positions. *ICGA Journal* 19, 3 (Sept. 1996), 181–183. <https://doi.org/10.3233/ICG-1996-19305>
- [11] Jeff Donahue, Yangqing Jia, Oriol Vinyals, Judy Hoffman, Ning Zhang, Eric Tzeng, and Trevor Darrell. 2014. DeCAF: A Deep Convolutional Activation Feature for Generic Visual Recognition. In *Proceedings of Machine Learning Research*, Vol. 32. PMLR, Beijing, 647–655. <http://arxiv.org/abs/1310.1531>
- [12] Fan Du, Nan Cao, Jian Zhao, and Yu-Ru Lin. 2015. Trajectory Bundling for Animated Transitions. In *Proceedings of the 33rd Annual ACM Conference on Human Factors in Computing Systems (CHI '15)*. ACM, New York, NY, USA, 289–298.
- [13] Daniel Engel, Lars HÄijttjenberger, and Bernd Hamann. 2012. A Survey of Dimension Reduction Methods for High-dimensional Data Analysis and Visualization. In *Visualization of Large and Unstructured Data Sets: Applications*

- in *Geospatial Planning, Modeling and Engineering – Proceedings of IRTG 1131 Workshop 2011 (OpenAccess Series in Informatics (OASISs))*, Vol. 27. Schloss Dagstuhl–Leibniz-Zentrum für Informatik, Dagstuhl, Germany, 135–149. <https://doi.org/10.4230/oasis.vluds.2011.135>
- [14] Dumitru Erhan, Yoshua Bengio, Aaron Courville, Pierre-Antoine Manzagol, Pascal Vincent, and Samy Bengio. 2010. Why Does Unsupervised Pre-training Help Deep Learning? *Journal of Machine Learning Research* 11 (2010), 625–660.
 - [15] O. Ersoy, C. Hurter, F.V. Paulovich, G. Cantareiro, and A. Telea. 2011. Skeleton-Based Edge Bundling for Graph Visualization. *IEEE Transactions on Visualization and Computer Graphics* 17, 12 (2011), 2364–2373. <https://doi.org/10.1109/TVCG.2011.233>
 - [16] Dénes Ferenc. 2016. Different Rubik’s Cube Solving Methods. <https://ruwix.com/the-rubiks-cube/different-rubiks-cube-solving-methods/> Accessed: 2019-02-28.
 - [17] Jessica Fridrich. 1997. My system for solving Rubik’s cube. <http://www.ws.binghamton.edu/fridrich/system.html> Accessed: 2019-02-25.
 - [18] Frederic Friedel. 2017. Fritz 16 – Freund und Trainer. ChessBase. <https://de.chessbase.com/post/fritz-16-freund-und-trainer> Accessed: 2019-11-04.
 - [19] David Gilday. 2019. How to build MindCub3r for Lego Mindstorms EV3. <https://www.mindcuber.com/mindcub3r/mindcub3r.html> Accessed: 2019-10-28.
 - [20] Andrej Gisbrecht, Alexander Schulz, and Barbara Hammer. 2015. Parametric nonlinear dimensionality reduction using kernel t-SNE. *Neurocomputing* 147 (Jan. 2015), 71–82. <https://doi.org/10.1016/j.neucom.2013.11.045>
 - [21] Philippe Hamel and Douglas Eck. 2010. Learning Features from Music Audio with Deep Belief Networks. In *Proceedings of the 11th International Society for Music Information Retrieval Conference*. International Society for Music Information Retrieval, Utrecht, Netherlands, 339–344.
 - [22] Pierre Havard. 2019. KingBase – a free chess games database, updated monthly. <https://www.kingbase-chess.net/> Accessed: 2019-11-07.
 - [23] Jianguan He and Chaomei Chen. 2017. Visualizing Temporal Patterns in Representation Data. In *VADL 2017: Workshop on Visual Analytics for Deep Learning*. IEEE, Phoenix, AZ, 4.
 - [24] Andreas Hinterreiter, Peter Ruch, Holger Stitz, Martin Ennemoser, Jörgen Bernard, Hendrik Strobel, and Marc Streit. 2019. ConfusionFlow: A model-agnostic visualization for temporal analysis of classifier confusion. *arXiv:1910.00969 [cs, stat]* (Oct. 2019). <http://arxiv.org/abs/1910.00969> arXiv: 1910.00969.
 - [25] G. E. Hinton. 2006. Reducing the Dimensionality of Data with Neural Networks. *Science* 313, 5786 (July 2006), 504–507. <https://doi.org/10.1126/science.1127647>
 - [26] Fred Hohman, Minsuk Kahng, Robert Pienta, and Duen Horng Chau. 2018. Visual Analytics in Deep Learning: An Interrogative Survey for the Next Frontiers. *IEEE Transactions on Visualization and Computer Graphics* 25, 8 (Jan. 2018), 2674–2693. <https://doi.org/10.1109/TVCG.2018.2843369>
 - [27] Danny Holten and Jarke J. van Wijk. 2009. Force-Directed Edge Bundling for Graph Visualization. *Computer Graphics Forum (EuroVis ’09)* 28, 3 (2009), 983–990. <https://doi.org/10.1111/j.1467-8659.2009.01450.x>
 - [28] J. D. Hunter. 2007. Matplotlib: A 2D Graphics Environment. *Computing in Science Engineering* 9, 3 (May 2007), 90–95. <https://doi.org/10.1109/MCSE.2007.55>
 - [29] Christophe Hurter, Ozan Ersoy, Sara I. Fabrikant, Tijmen R. Klein, and Alexandru C. Telea. 2013. Bundled Visualization of Dynamic Graph and Trail Data. *IEEE Transactions on Visualization and Computer Graphics* 20, 8 (2013), 1141–1157. <https://doi.org/10.1109/TVCG.2013.246>
 - [30] Justin Jaffray. 2017. CubeSolves. <http://cubesolv.es/> Accessed: 2019-02-25.
 - [31] Brittany Kondo and Christopher Collins. 2014. DimpVis: Exploring Time-varying Information Visualizations by Direct Manipulation. *IEEE Transactions on Visualization and Computer Graphics (InfoVis ’14)* 20, 12 (2014), 2003–2012. <https://doi.org/10.1109/TVCG.2014.2346250>
 - [32] Daniel Kunkle and Gene Cooperman. 2007. Twenty-six moves suffice for Rubik’s cube. In *Proceedings of the 2007 international symposium on Symbolic and algebraic computation – ISSAC ’07*. ACM Press, Waterloo, Ontario, Canada, 235. <https://doi.org/10.1145/1277548.1277581>
 - [33] Yann LeCun. 2005. The MNIST database of handwritten digits. <http://yann.lecun.com/exdb/mnist/>
 - [34] Yann LeCun, Yoshua Bengio, and Geoffrey Hinton. 2015. Deep learning. *Nature* 521, 7553 (May 2015), 436–444. <https://doi.org/10.1038/nature14539>
 - [35] Fritz Lekschas, Michael Behrisch, Benjamin Bach, Peter Kerpedjiev, Nils Gehlenborg, and Hanspeter Pfister. 2019. Pattern-Driven Navigation in 2D Multiscale Visualizations with Scalable Insets. *bioRxiv* (July 2019). <https://doi.org/10.1101/301036>
 - [36] Lucas Liberacki and Tom Brannan. 2015. Rubik’s Cube Solver coded in Python. <https://github.com/CubeLuke/Rubiks-Cube-Solver> Accessed: 2019-02-28.
 - [37] Wei-Li Lu, Yu-Shuen Wang, and Wen-Chieh Lin. 2014. Chess Evolution Visualization. *IEEE Transactions on Visualization and Computer Graphics* 20, 5 (May 2014), 702–713. <https://doi.org/10.1109/TVCG.2014.2299803>

- [38] Shotaro Makisumi. 2012. Speedsolving.com Wiki. Category: 3x3x3 methods. https://www.speedsolving.com/wiki/index.php/Category:3x3x3_methods Accessed: 2019-02-28.
- [39] Yi Mao, Joshua Dillon, and Guy Lebanon. 2007. Sequential Document Visualization. *IEEE Transactions on Visualization and Computer Graphics* 13, 6 (Nov. 2007), 1208–1215. <https://doi.org/10.1109/TVCG.2007.70592>
- [40] Leland McInnes, John Healy, and James Melville. 2018. UMAP: Uniform Manifold Approximation and Projection for Dimension Reduction. *arXiv:1802.03426 [cs, stat]* (Dec. 2018). <http://arxiv.org/abs/1802.03426> arXiv: 1802.03426.
- [41] Volodymyr Mnih, Koray Kavukcuoglu, David Silver, Andrei A. Rusu, Joel Veness, Marc G. Bellemare, Alex Graves, Martin Riedmiller, Andreas K. Fidjeland, Georg Ostrovski, Stig Petersen, Charles Beattie, Amir Sadik, Ioannis Antonoglou, Helen King, Dharshan Kumaran, Daan Wierstra, Shane Legg, and Demis Hassabis. 2015. Human-level control through deep reinforcement learning. *Nature* 518, 7540 (Feb. 2015), 529–533. <https://doi.org/10.1038/nature14236>
- [42] Abdel-rahman Mohamed, Geoffrey Hinton, and Gerald Penn. 2012. Understanding how Deep Belief Networks perform acoustic modelling. In *2012 IEEE International Conference on Acoustics, Speech and Signal Processing (ICASSP)*. IEEE, Kyoto, Japan, 4273–4276. <https://doi.org/10.1109/ICASSP.2012.6288863>
- [43] F. Pedregosa, G. Varoquaux, A. Gramfort, V. Michel, B. Thirion, O. Grisel, M. Blondel, P. Prettenhofer, R. Weiss, V. Dubourg, J. Vanderplas, A. Passos, D. Cournapeau, M. Brucher, M. Perrot, and E. Duchesnay. 2011. Scikit-learn: Machine Learning in Python. *Journal of Machine Learning Research* 12 (2011), 2825–2830.
- [44] Lars Petrus. 1997. Solving Rubik’s Cube for speed. <https://lar5.com/cube/> Accessed: 2019-11-20.
- [45] V. Peysakhovich, C. Hurter, and A. Telea. 2015. Attribute-driven edge bundling for general graphs with applications in trail analysis. In *2015 IEEE Pacific Visualization Symposium (PacificVis)*. IEEE, Hangzhou, China, 39–46. <https://doi.org/10.1109/PACIFICVIS.2015.7156354>
- [46] Pavlin G. PoliÄžar, Martin StraÄžar, and BlaÄž Zupan. 2019. openTSNE: a modular Python library for t-SNE dimensionality reduction and embedding. *bioRxiv* (Aug. 2019). <https://doi.org/10.1101/731877>
- [47] P. E. Rauber, S. G. Fadel, A. X. FalcÄo, and A. C. Telea. 2017. Visualizing the Hidden Activity of Artificial Neural Networks. *IEEE Transactions on Visualization and Computer Graphics* 23, 1 (Jan. 2017), 101–110. <https://doi.org/10.1109/TVCG.2016.2598838>
- [48] Tomas Rokicki, Herbert Kociemba, Morley Davidson, and John Dethridge. 2010. God’s Number is 20. <http://www.cube20.org/> Accessed: 2019-11-02.
- [49] Tobias Schreck, Tatiana TekuÄqovÄq, JÄurn Kohlhammer, and Dieter Fellner. 2007. Trajectory-based visual analysis of large financial time series data. *ACM SIGKDD Explorations Newsletter* 9, 2 (2007), 30–37.
- [50] David Silver, Thomas Hubert, Julian Schrittwieser, Ioannis Antonoglou, Matthew Lai, Arthur Guez, Marc Lanctot, Laurent Sifre, Dharshan Kumaran, Thore Graepel, Timothy Lillicrap, Karen Simonyan, and Demis Hassabis. 2018. A general reinforcement learning algorithm that masters chess, shogi, and Go through self-play. *Science* 362, 6419 (Dec. 2018), 1140–1144. <https://doi.org/10.1126/science.aar6404>
- [51] Christian Steinparz, Andreas Hinterreiter, Holger Stitz, and Marc Streit. 2019. Visualization of Rubik’s Cube Solution Algorithms. In *EuroVis Workshop on Visual Analytics (EuroVA)*. The Eurographics Association, Porto, Portugal, 5. <https://doi.org/10.2312/eurova.20191119>
- [52] Holger Stitz, Samuel Gratzl, Wolfgang Aigner, and Marc Streit. 2016. ThermalPlot: Visualizing Multi-Attribute Time-Series Data Using a Thermal Metaphor. *IEEE Transactions on Visualization and Computer Graphics* 22, 12 (2016), 2594–2607. <https://doi.org/10.1109/TVCG.2015.2513389>
- [53] J. B. Tenenbaum. 2000. A Global Geometric Framework for Nonlinear Dimensionality Reduction. *Science* 290, 5500 (Dec. 2000), 2319–2323. <https://doi.org/10.1126/science.290.5500.2319>
- [54] Teodus. 2017. AlgExplorer: command-line utility to assist in alg searching. <https://www.speedsolving.com/forum/threads/65189/> Accessed: 2019-02-28.
- [55] Deniz (<https://github.com/dn1z>). 2018. pgn2gif. <https://github.com/dn1z/pgn2gif> Accessed: 2019-11-07.
- [56] Henry (<https://math.stackexchange.com/users/6460/henry>). 2017. How is the distance of two random points in a unit hypercube distributed? Mathematics Stack Exchange. <https://math.stackexchange.com/q/1985698> Accessed: 2019-10-22.
- [57] S. van den Elzen, D. Holten, J. Blaas, and J.J. van Wijk. 2016. Reducing Snapshots to Points: A Visual Analytics Approach to Dynamic Network Exploration. *IEEE Transactions on Visualization and Computer Graphics* 22, 1 (Jan. 2016), 1–10. <https://doi.org/10.1109/TVCG.2015.2468078>
- [58] Laurens van der Maaten and Geoffrey Hinton. 2008. Visualizing Data using t-SNE. *Journal of Machine Learning Research* 9, Nov (2008), 2579–2605.
- [59] Laurens van der Maaten, Eric Postma, and Jaap van den Herik. 2009. *Dimensionality Reduction: A Comparative Review*. Technical Report TR 2009-005. Tilburg University, Tilburg, Netherlands. 36 pages.
- [60] Matthew O. Ward and Zhenyu Guo. 2011. Visual Exploration of Time-Series Data with Shape Space Projections. *Computer Graphics Forum* 30, 3 (June 2011), 701–710. <https://doi.org/10.1111/j.1467-8659.2011.01919.x>
- [61] Martin Wattenberg. 2016. Thinking Machine 6. <http://www.bewitched.com/chess/> Accessed: 2019-11-04.

- [62] Yu Zheng. 2015. Trajectory Data Mining: An Overview. *ACM Transactions on Intelligent Systems and Technology* 6, 3 (May 2015), 1–41. <https://doi.org/10.1145/2743025>
- [63] Biao Zhu and Wei Chen. 2016. Performance Histogram Curve: Abstractive Visualization and Analysis of NBA Games. *International Journal of Software & Informatics* 10, 3 (2016), 11. <https://doi.org/10.21655/ijsi.1673-7288.00231>